Journal of Materials Chemistry A

Accepted Manuscript

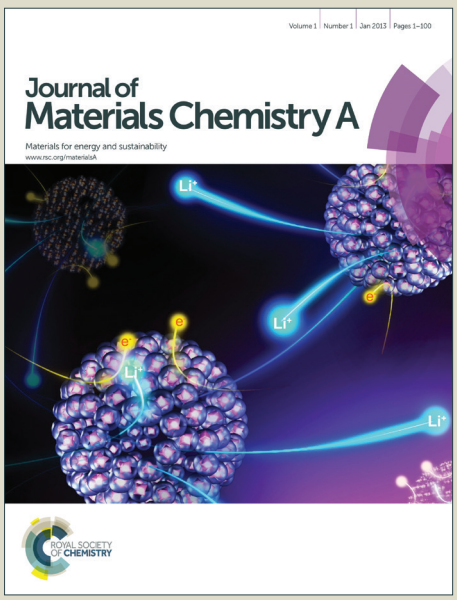

ROYAL SOCIETY OF CHEMISTRY

www.rsc.org/materialsA

Journal of Materials Chemistry

RSCPublishing

ARTICLE

Hierarchically Porous Materials Built of Fe-silicalite Nanobeads†

Cite this: DOI: 10.1039/x0xx00000x

K.A. Sashkina,[a,c,*] N.A. Rudina,[a] A.I. Lysikov,[a,b] A.B. Ayupov[a] and E.V. Parkhomchuk[a,b,c]

Received 00th January 2014,
Accepted 00th January 2014

DOI: 10.1039/x0xx00000x

www.rsc.org/

Hierarchically porous zeolite materials built of close and random packed uniform Fe-silicalite nanobeads were synthesized. The desired assembly of nanobeads was achieved by the centrifugation and sedimentation of nanozeolite suspension followed by drying and calcination. Micro/meso/macroporous Fe-silicalite material with spongy texture built of closely packed nanocrystals was designed using polystyrene latex as a supramolecular template. Large Fe-silicalite microbeads were synthesized to compare their structure with nanocrystalline materials. The synthesized samples were characterized by laser diffraction analysis, X-ray diffraction, scanning and transmission electron microscopy, energy-dispersive X-ray spectroscopy, argon and nitrogen adsorption measurements, inductively coupled plasma optical emission spectrometry, UV visible diffuse reflectance spectroscopy and temperature-programmed desorption of ammonia. Fe-silicalite nanozeolite materials have shown high crystallinity, micro- and meso/macropore surface area and high specific pore volume. Pellets built of closely packed nanocrystals have exhibited a good mechanical stability in benzene and water. Calcined Fe-silicalite materials built of nanobeads were observed to contain highly dispersed ferric clusters no more than 1 nm in size. The 3 nm-ferric clusters in zeolitic microbeads resulted in the appearance of Lewis acid sites with medium strength, which are absent in nanobeads. Catalytic performance of hierarchically porous Fe-silicalites was studied in total oxidation of clarithromycin lactobionate by H_2O_2 at 323 K compared with Fe-silicalite microspheres. Hierarchical Fe-silicalites are more efficient catalysts vs Fe-silicalite microbeads due to increasing catalytic sites accessibility.

Introduction

Zeolites represent a unique class of crystalline aluminosilicates with ordered micropores of molecular dimensions (<2 nm). Zeolites find wide applications as adsorbents and catalysts because of their specific structure resulting in size/shape-selective and acidic properties.[1]

Design of zeolite materials containing transition metal compounds is of great importance for the development of catalysts for green liquid phase oxidation.[2] Zeolite matrices stabilizes active metal species in the highly dispersed state and protects them against the deactivation.[3] Iron-containing zeolites are effective catalysts both for partial and total oxidation of organic compounds by nontoxic reagents (O_2, H_2O_2) under mild conditions. The development of green processes for selective hydrocarbon oxidation using Fe-zeolites seemed to be fruitful. Zeolite Fe-ZSM-5 has been recently reported to display significant catalytic activity for selective oxidation of methane and ethane by hydrogen peroxide at low temperatures.[4,5] Total oxidation by means of heterogeneous Fenton-like systems including Fe-zeolite/H_2O_2 is a topical process for water decontamination.[6] The zeolite Fe-ZSM-5 was shown to be an effective catalyst for total oxidation of a wide range of organic substrates.[7]

In recent decade, pharmaceutically active compounds (PhACs) and endocrine disrupting chemicals (EDCs) in the ng/L–mg/L range have been detected worldwide in aquatic environment and drinking water and have been acknowledged to constitute a health risk for humans and ecosystems.[8-10] Since PhACs removal on sewage treatment plants is not sufficiently efficient, advanced water decontamination processes are required.[11,12] Environmentally safe Fe-zeolite/H_2O_2 systems seem to be promising for total oxidation of organic pollutants in low concentrations during water post-treatment due to high adsorption capacity of zeolite surface enhancing the interaction between the substrate and ȮH radicals formed on the iron-containing catalytic sites at zeolite surface.[13]

The key problem of zeolite catalysts is intracrystalline diffusion constraints resulting in low utilization of zeolite active surface especially in reactions involving large molecules.[14] To increase accessibility of active zeolite surface, two main approaches are applied: decreasing the size of zeolite particles or creating hierarchical pore architecture combining micropores and transport meso/macropores.[15-17] The combination of these two approaches represents designing hierarchically porous materials built of zeolite nanocrystals. Obviously, the ordered hierarchical porosity of new materials, including zeolites, may significantly enhance catalytic and adsorption properties as well as expand their application range far

beyond the traditional one.[18,19] The desired texture of zeolites can be achieved by controlling crystal size and a manner of zeolite assembly. There are a number of strategies available for assembling zeolite nanocrystals into hierarchically porous materials. Templating approach is widely used for the fabrication of a diverse structural organization of nanozeolites. Filling arrays composed of closely packed monodisperse polymer microspheres with nanozeolites followed by calcination of obtained composites have been allowed producing 3D ordered macroporous zeolite materials.[20,21] Microspheres consisting of nanozeolites have been synthesized by the polymerization-induced colloid aggregation (PICA) method. For example, polymerization of urea and formaldehyde have been carried out in nanozeolite suspension to produce zeolite/polymer beads, the calcination of composite resulting in the formation of hierarchically porous zeolite microspheres.[22] Zeolite bodies built of uniform closely packed nanocrystals have been obtained by transforming amorphous silica grains impregnated with ZSM-5 precursors or seeds under hydrothermal conditions.[23]

The present study describes the synthesis of hierarchically porous materials consisting of uniform Fe-silicalite nanobeads with close, random and spongy packing of initial building blocks. The desired assembly of nanozeolites has been achieved by the sedimentation, centrifugation and template-directed synthesis. Interestingly, that closely packed Fe-silicalite nanocrystals have formed pellets ranged from 5 to 10 mm exhibiting a good mechanical stability in benzene and water. The effect of zeolite morphology on the state of iron and material acidity has been studied. Catalytic performance of hierarchically porous Fe-silicalite has been compared with Fe-silicalite microbeads in total peroxide oxidation of clarithromycin lactobionate, belonging to the group of macrolide antibiotics.

Experimental

Materials

Tetrapropylammonium hydroxide (TPAOH, 25 wt. % solution in water, Acros), tetraethylorthosilicate (TEOS, ≥98%, Angara-reactive, $Fe(NO_3)_3{\cdot}9H_2O$ (≥99%, Merck) and ethanol (EtOH, 95%, Pharmaceya) were applied for the synthesis of hierarchically porous nanozeolite bodies. Silica (fumed, ≥99 %, Aldrich) and tetrapropylammonium bromide (98 %, Aldrich) were used for producing zeolite microbeads. Styrene monomer (Angara-reactive, inhibited with 1% hydroquinone), sodium hydroxide (NaOH, 98%, Tellura) and potassium persulfate (≥99%, Acros) were used for obtaining latex as a macropore-generating agent. Clarithromycin lactobionate (Abbott Laboratories) was applied as a substrate for total catalytic oxidation by hydrogen peroxide (30% aqueous solution, Baza №1 Khimreactivov).

Synthesis of Fe-silicalite Materials

Nanozeolite suspensions for building hierarchically porous zeolite materials were synthesized as follows. 10 ml of TEOS diluted with 10 ml of ethanol was added at once to 20 ml of TPAOH (12.5 wt. %) under vigorous stirring for 10 min, then 0.20 g of $Fe(NO_3)_3{\cdot}9H_2O$ dissolved in 1 ml of distilled water was added dropwise. After stirring for 20 min, clear light-yellow suspension having 1.00 SiO_2 : 0.14 $(TPA)_2O$: 0.005 Fe_2O_3: 3.89 Et_2O : 21.7 H_2O molar composition was formed. The resultant gel was placed in a Teflon-lined stainless steel autoclave and subjected to the hydrothermal treatment in an oven at 363 K for 7 days. Milky Fe-silicalite suspensions produced were purified in a series of three steps consisting of centrifugation at relative acceleration of 1500 g for 5 h, followed by removal of mother liquor and redispersion in distilled water under ultrasonication.

For the formation of zeolite pellets built of closely packed nanocrystals, zeolite suspension was centrifuged at the relative acceleration of 1500 g for 24 h and dried at 298 K for 2 days. A part of nanozeolite pellets was left for the analysis by UV-vis diffuse reflectance spectroscopy. Another part of the zeolite was calcined at 773 K for 5 h.

Randomly packed nanocrystals were fabricated by the procedure described above, but without zeolite centrifugation after purification stage. Fe-silicalite suspension was only dried at 323 K for 12 h. A part of as-synthesized material was left for the analysis by UV-vis diffuse reflectance spectroscopy. Another part of the zeolite was calcined at 773 K for 5 h.

For spongy packing of Fe-silicalite nanocrystals the synthesis was modified via using latex as a supramolecular template. Polystyrene (PS) latex (5 wt. %) was obtained following a procedure reported elsewhere.[24] 10 ml of latex was added to precursor solution containing 10 ml of TEOS, 10 ml of ethanol, 10 ml of TPAOH (25 wt. %) and 0.20 g of $Fe(NO_3)_3{\cdot}9H_2O$ under vigorous stirring for one hour. The resultant gel was placed in a Teflon-lined stainless steel autoclave and subjected to the hydrothermal treatment in an oven at 363 K for 7 days. Zeolite/PS composite generated from the gel containing latex was rinsed with distilled water and dried at ambient temperature for 24 h. A part of the composite was left for the analysis by UV-vis diffuse reflectance spectroscopy. Another part of zeolite/PS composite was calcined at 773 K for 5 h.

The synthesis of large Fe-silicalite microbeads as a reference sample was performed at the following chemical composition of precursor solution: 1 SiO_2:0.1 Na_2O:0.055 $(TPA)_2O$: 0.01 Fe_2O_3: 35 H_2O. In a typical synthesis procedure, 5.00 g of silica was gradually added to an aqueous solution containing 0.67 g NaOH and 2.44 g of TPABr under magnetic stirring at ambient temperature. After stirring for 10 min, 0.65 g of $Fe(NO_3)_3{\cdot}9H_2O$ dissolved in 1 ml of distilled water was added dropwise to obtained milky suspension. After further stirring for 5 min, the gel mixture was transferred to a Teflon-lined stainless steel autoclave. The autoclave was maintained in an oven at 433 K for 72 h. After the hydrothermal treatment, the solid product was filtered, rinsed with distilled water and dried at 373 K for 12 h. A part of zeolite powder was left for the analysis by UV-vis diffuse reflectance spectroscopy. Another part was calcined at 773 K for 5 h.

Characterization

The hydrodynamic diameters of zeolite particles in suspensions were determined with a Malvern Mastersizer-2000 particle size analyser with an incident laser wavelength of 470 nm and an output power of 0.3 mW. Powder X-ray diffraction (XRD) patterns were recorded from a Siemens D500 diffractometer equipped with a Cu Kα radiation (λ = 0.154 nm). The chemical composition of the samples was determined by inductively coupled plasma optical emission spectrometry (ICP-OES). Scanning electron microscopy (SEM) images were taken with a JEOL JSM-6460LV microscope at an operating voltage of 15–20 kV. Energy Dispersive X-ray Spectrometry (EDS) and transmission electron microscopy (TEM) images were obtained by a JEOL JEM-2010 microscope operating at 200 kV. Nitrogen and argon adsorption-desorption isotherms were measured with a Quantachrome Autosorb-6B-Kr surface area analyser at liquid N_2 and Ar temperature — 77 and 87 K, respectively. Prior to the analysis, samples were outgassed at 573 K for 10 h. Specific surface areas were determined applying BET equation[25]. Pore size distributions were estimated by the BJH[26] and NLDFT[27] methods. Micropore volume and external surface area were also calculated by means of α_s–method with using the isotherm of adsorption of N_2 and Ar on the reference LiChrospher Si-1000 silica gel, reported in the literature.[28,29] UV-vis diffuse reflection

(DR) spectra were recorded on a Shimadzu UV-2501 PC in wavenumber range 11000–54000 cm^{-1} at 298 K. The acidities of the samples were tested by TPD of ammonia using lab-scale calibrated equipment. Ammonia quantity signal was measured by quadrupole mass spectrometer HiCube RGA100 and temperature control was operated by temperature controller Termodat 13KT2/5T supplying continuous sample heat rate.

Catalytic tests

Fe-silicalites were tested in H_2O_2 decomposition in a 5-mL thermostatted glass batch reactor agitated with magnetic stirrer. Kinetic curves of O_2 emission were recorded by the barometric device at the following conditions: volume of liquid phase was 2.5 ml, T = 323 K, Fe-silicalite catalyst concentration – 20 g/L, initial concentrations of H_2O_2 were 1 M.

Total catalytic oxidation of clarithromycin lactobionate (CL) by hydrogen peroxide was carried out at 323 K in a 100-mL thermostatted glass batch reactor agitated with magnetic stirrer. The reactor was connected to mass spectrometer HiCube RGA100. In the experiment, volume of liquid phase was 50 ml, Fe-silicalite catalyst concentration – 20 g/L, initial concentrations of CL and H_2O_2 were 300 mg/L and 1 M, respectively.

Results and discussion

Representative particle size distribution of the initial building units in suspensions for the further formation of materials with closely and randomly packed nanoparticles is shown in Fig. 1. Particles with a mean diameter of about 170 nm and narrow size distribution were observed by dynamic light scattering.

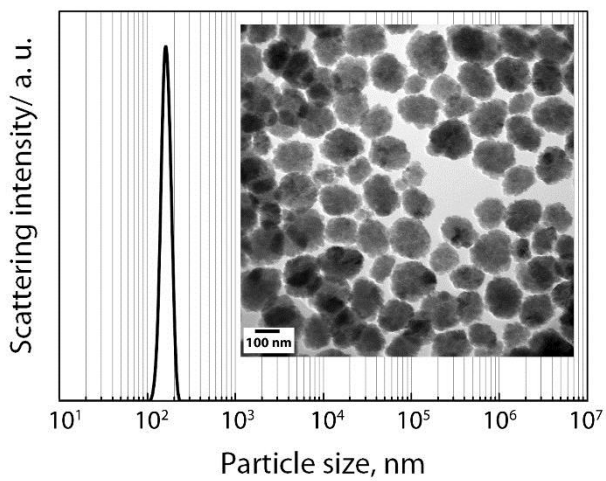

Fig. 1. Dynamic light scattering data for Fe-silicalite suspensions. The inset shows the TEM image of Fe-silicalite nanobeads.

According to TEM image in the inset of Fig. 1 zeolite particles have spheroidal shape and therefore they are referred to as nanobeads here. Fe-silicalite nanobeads for producing hierarchically porous materials were found to be single crystals by HRTEM images, since inseverable parallel planes extend across each crystal (see Fig. 2a).

Hierarchically porous materials built of closely and randomly packed Fe-silicalite nanobeads (Fig. 3 b, d) were formed by means of centrifugation and drying of Fe-silicalite suspension, respectively, followed by calcination. For designing micro/meso/macroporous Fe-silicalite materials with spongy texture (Fig. 3c), the synthesis was modified via adding polystyrene latex as a template during gel formation. The following hydrothermal treatment of the gel induced creating Fe-silicalite/polystyrene composite, calcination of that resulted in the formation of spongy texture. Large FeZSM-5 microbeads with the average size of 5 μm have been also designed for comparing structural features of nanozeolite materials (Fig. 3a).

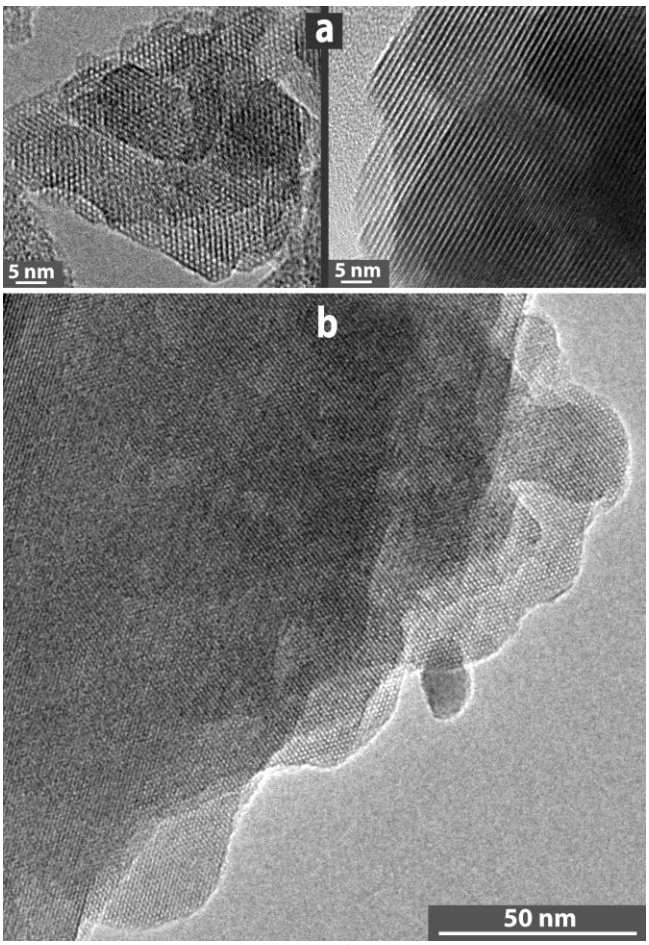

Fig. 2. High-resolution TEM images of calcined Fe-silicalite nanocrystals – initial building blocks for producing hierarchically porous materials (a) and as-synthesized Fe-silicalite microbeads (c).

Hierarchically porous bodies with random and spongy packing of nanobeads represent aggregates ranged from 10 to 50 μm according to the SEM image (Fig. 4). The formation of a spongy texture during the synthesis can be accounted for spontaneous aggregation of PS spheres in basic reaction media followed by the growth of nanozeolites in the gaps between aggregated PS spheres. Macropores in zeolite materials with a spongy texture are formed after burning assemblies of polystyrene spheres from zeolite/PS composite.

Special attention should be given to discussing Fe-silicalite pellets consisting of closely packed nanobeads. Fig. 5 shows a photograph of opalescent Fe-silicalite pellets ranged from 5 to 10 mm on a Petri dish. White calcined Fe-silicalite pellets became transparent under immersion in benzene (see video ESI) and then no redispersion of pellets in solvents were observed for a month.

The XRD patterns of all materials (Fig. 6) are typical for highly crystalline MFI type zeolites. The relative crystallinity was calculated from peaks area in the $22^{o}<2\theta<25^{o}$ region using Fe-silicalite microbeads as a reference (Table 1). Calcined hierarchically porous pellets built of closely packed Fe-silicalite nanobeads showed a good mechanical stability during ultrasonication in solvents stated above for an hour and therefore are of particular interest for practical applications.

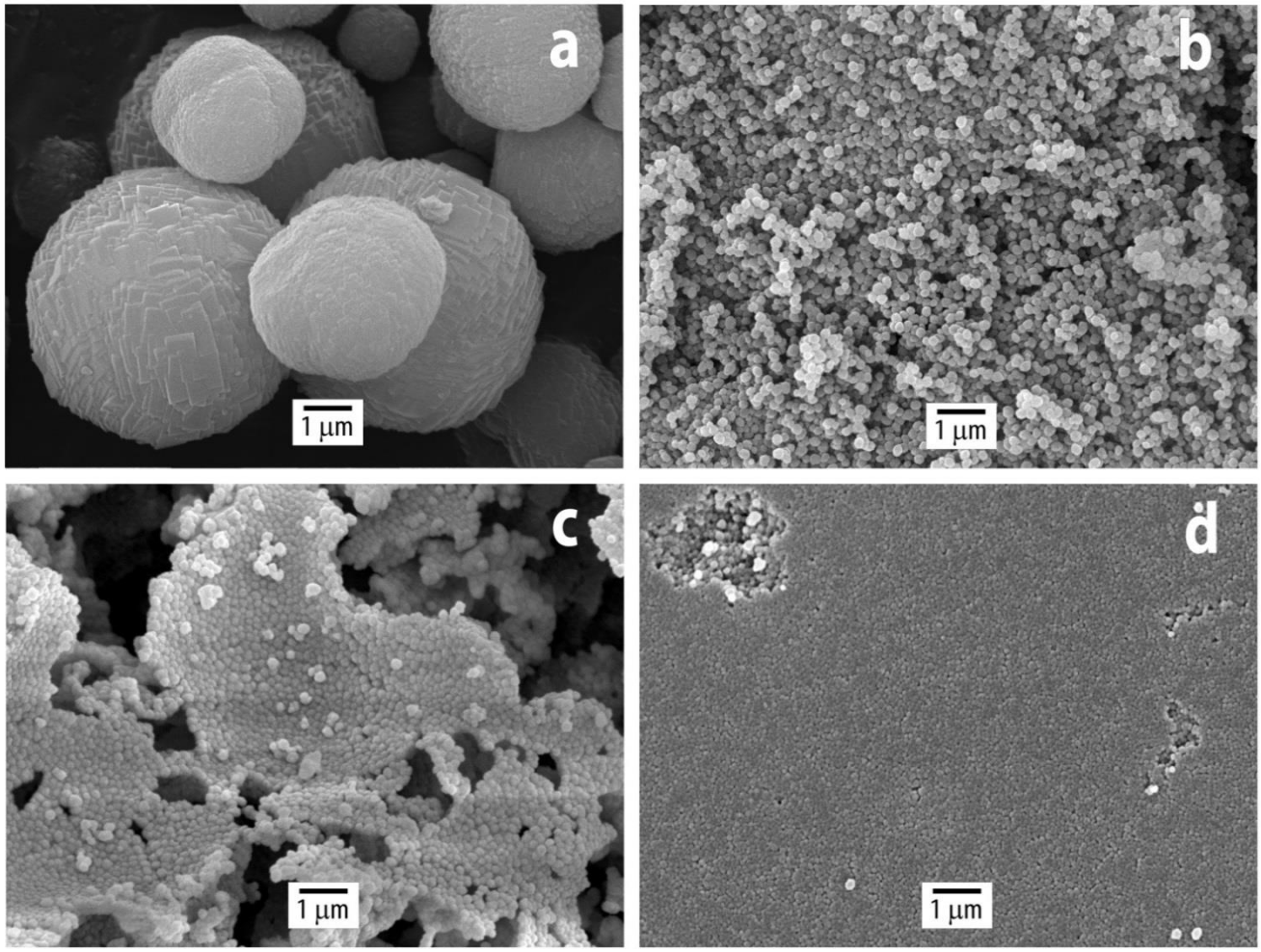

Fig. 3. SEM images of calcined zeolites Fe-ZSM-5: microbeads (a), zeolite materials with random (b), spongy (c) and close (d) packing of nanobeads.

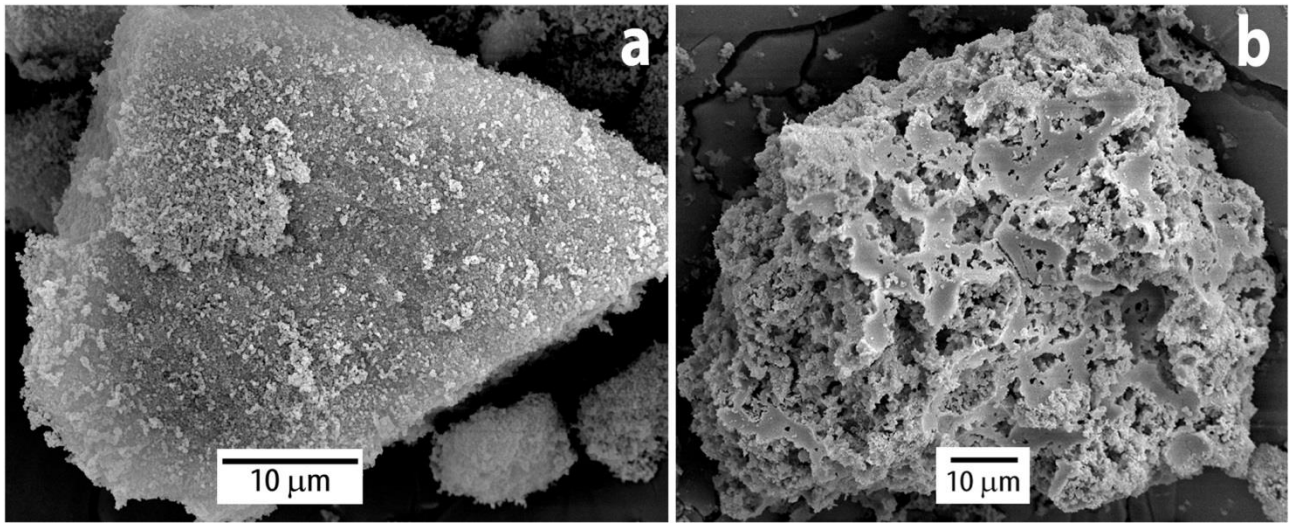

Fig. 4. SEM image of calcined zeolite materials with random (a) and spongy (b) packing of Fe-silicalite nanobeads.

Fig. 5. Photograph of as-synthesized closely packed FeZSM-5 nanozeolite pellets on a Petri dish.

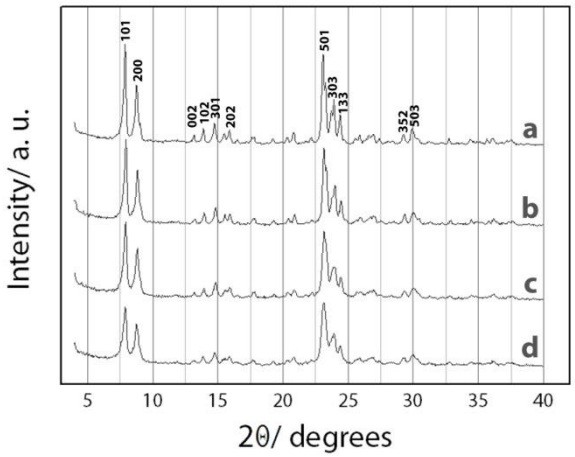

Fig. 6. XRD patterns of calcined Fe-silicalite materials: microbeads (a), zeolite bodies with random (b), spongy (c) and close (d) packing of nanobeads.

Table 1. Physicochemical properties of Fe-silicalite materials.

Fe-silicalite sample	S_{BET}, m^2/g		S_{Ext}, m^2/g		V_{total}, cm^3/g		V_{micro}, cm^3/g		XRD crystallinity, %	Fe content, %	Total NH_3 adsorption capacity, mmol/g	Strong acidity related to h-peak (620 K), mmol/g
	N_2	Ar	N_2	Ar	N_2	Ar	N_2	Ar				
Microbeads	419	380	72	79	0.21	0.20	0.14	0.11	100	1.95	0.20	0.08*
Nanobeads random packing	518	516	86	178	0.63	0.64	0.20	0.15	92	1.28	0.14	0.04
Nanobeads spongy packing	545	499	224	222	0.59	0.72	0.14	0.12	95	1.06	0.16	0.04
Nanobeads close packing	551	369	204	36	0.75	0.39	0.13	0.12	92	1.28	0.12	0.05

* The peak was shifted to the lower desorption temperature – 560 K.

Textural characteristics of calcined Fe-silicalite materials with different morphologies were determined by nitrogen and argon adsorption (Table 1). All zeolite samples exhibit high BET surface area (369-550 m^2/g) and micropore volume (0.11-0.20 cm^3/g) to be in accordance with their good XRD crystallinity (Fig. 3). External surface area and total pore volume of hierarchically porous zeolite bodies are much higher compared with large zeolite microbeads (Table 1). Nitrogen and argon adsorption/desorption isotherms and pore size distributions of zeolite materials are represented in Fig. 7. Isotherms measured on all samples have a clear uptake at low relative pressure corresponding to filling micropores with nitrogen or argon. For zeolite microbeads, the initial step increase followed by horizontal adsorption and desorption branches is to be the characteristic feature of Type I isotherm typical for microporous materials. For hierarchically porous zeolite materials, isotherms show the hysteresis loop at high relative pressure ranges indicating the presence of large mesopores. Pore size distributions estimated by the BJH (N_2) and NLDFT (Ar) methods can be seen in Fig. 7 e, f. It should be emphasized that using argon as an adsorbate for analysing pore size distribution enables to obtain data for micropores.[27] Distribution curves for all samples were observed to have a narrow peak at about 5.5 Å corresponding to framework type MFI. Also we observed less intensive peak on pore size distribution at 8-9 Å, which was previously reported to be characteristic for MFI micropore structure and which could be explained by phase transformation of adsorbate.[30,31] Pore size distributions in mesopore region directly depend on morphology of zeolite materials. For random and spongy packing of Fe-silicalite nanobeads, one can see a wide mesopore size distribution from 10 to 80 nm, the major part of mesopores being in the ranges 40-70 nm and 10-40 nm for random and spongy packing, respectively. Distribution curves for Fe-silicalite pellets exhibit a sharp maximum at 25 nm confirming close packing of nanobeads in the bulk of zeolite material. According to BJH calculation, Fe-silicalite microbeads contain a bit of mesopores in the range 10-20 nm appeared to be defects of structure, which can be seen in TEM images of the crystal (Fig. 2 b).

Zeolite materials were revealed to contain 1-2 % of iron according to the chemical analyses (Table 1). EDS mapping indicated uniformly distributed iron species inside Fe-silicalite crystals (Fig. 8 a).

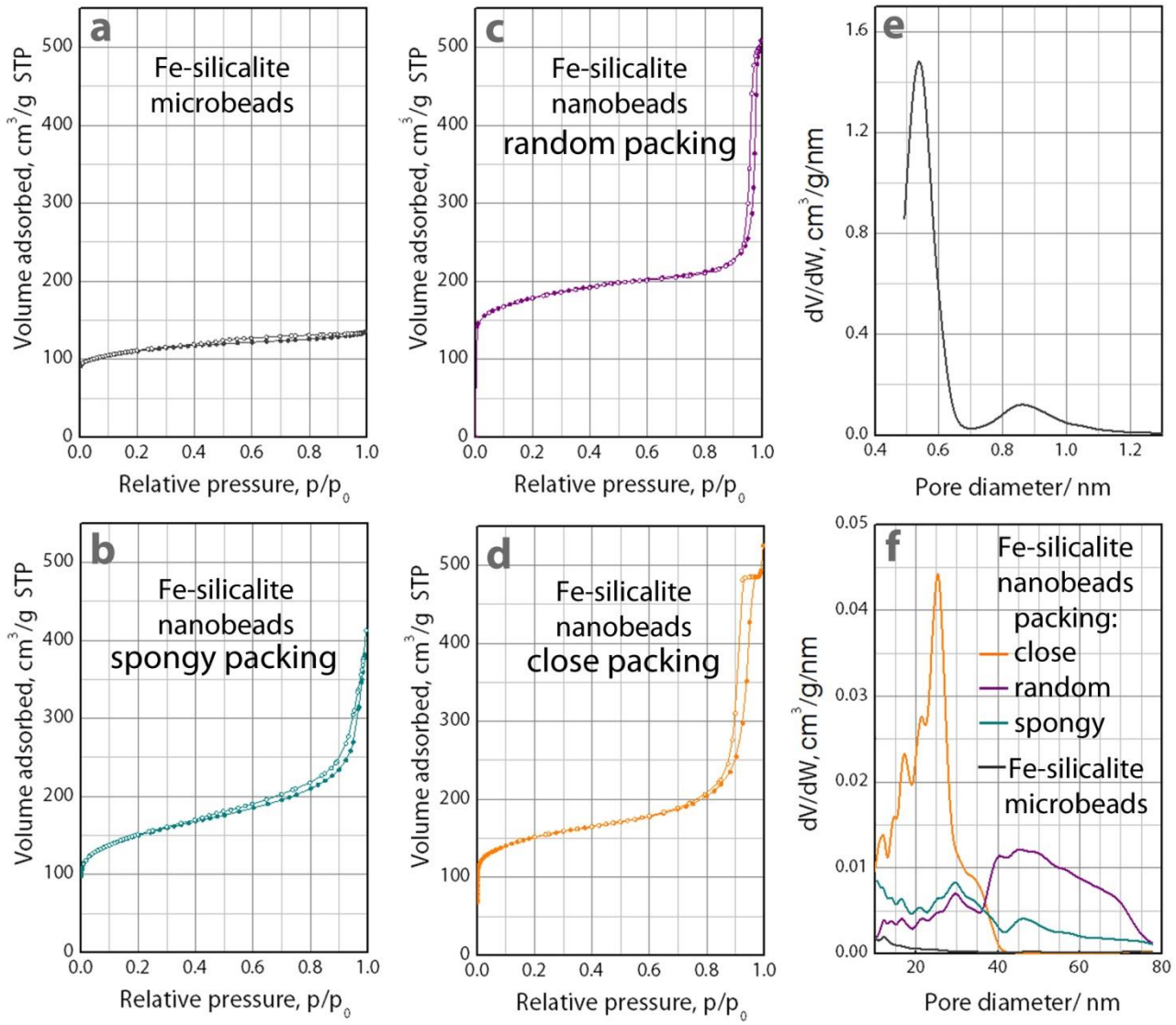

Fig. 7. Nitrogen adsorption/desorption isotherms of Fe-silicalite materials (a–d). Typical micropore size distribution for all samples (e) estimated by NLDFT (Ar), and mesopore size distributions (f) estimated by BJH (N_2) method.

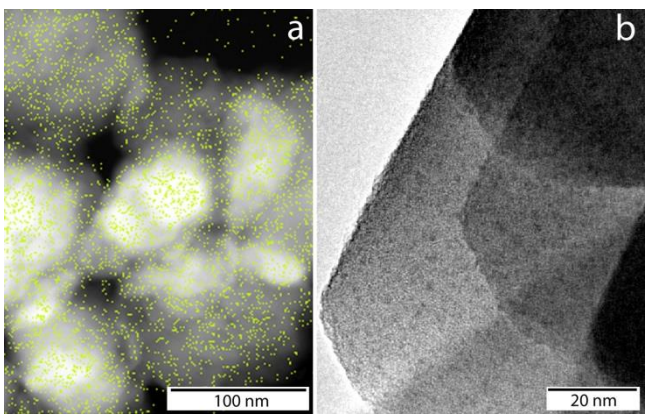

Fig. 8. Distribution of iron in calcined Fe-silicalite nanocrystals according EDS analysis (a), TEM image of calcined Fe-silicalite microbeads (b).

The state of iron species in as-synthesized and calcined Fe-silicalite materials were studied by UV-visible DR spectroscopy. A strong absorption in the 30,000-50,000 cm^{-1} region was observed for all zeolite materials (Fig. 9 a), two clearly distinguished peaks around 41,000 and 46,000 cm^{-1} corresponding to O^{2-} ligand→metal charge transfer $t_1 \rightarrow e$ and $t_1 \rightarrow t_2$ involving Fe^{3+} in tetrahedral or octahedral oxygen surroindings.[24] Spectra for as-synthesized Fe-silicalite microbeads and bodies built of randomly and closely packed nanobeads were found to have three extremely weak peaks (see insert of Fig. 9 a) around 22,700, 24,600 and 26,800 cm^{-1} resulted from forbidden d-d transitions $^6A_1 \rightarrow {}^4T_1$, $^6A_1 \rightarrow {}^4T_2$, and sum of $^6A_1 \rightarrow {}^4A_1$ and $^6A_1 \rightarrow {}^4E$ of the isolated high-spin Fe^{3+} ions in tetrahedral oxygen coordination (see Tanabe-Sugano diagram for d^5 electron configuration). In sum, UV-visible DR spectra of white as-synthesized zeolite materials being in a good agreement with crystal field theory and the literature data for Fe-silicalites[32] indicate that Fe^{3+} ions occupy tetrahedral lattice positions.

UV-visible DR spectra of calcined zeolite materials are seen to be clearly modified relative to those of as-synthesized samples (Fig. 9 a), the difference between reflection spectra being exhibited in Fig. 9 b. Intensive peak of absorption arisen at 35,000-36,000 cm^{-1} indicates the formation of clusters of several nm in size with Fe^{3+} in octahedral complexes.[32,33]

The presence of iron in both tetrahedral and octahedral oxygen coordination in turn induced broadening of d–d peaks because of difference between magnitudes of ligand field splitting energy. Note that no formation of large ferric aggregates of tens nm in size in all materials was observed due to the absence of absorption at 20,000 cm^{-1}.[34,35] Thus, calcination resulted in partial Fe^{3+} migration from zeolite lattice to form small clusters of iron species in extraframework positions.

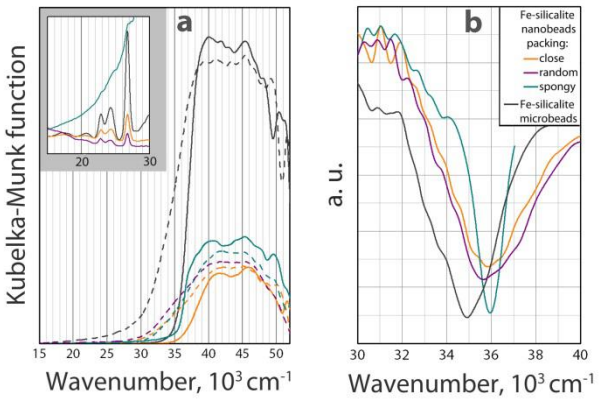

Fig. 9. UV-visible DR spectra of Fe-silicalite materials (a) and the differences between spectra of as-synthesized and calcined samples (b).

It should be noted that the absorption band of iron clusters consisting the calcined zeolite particles shifts to the blue (Fig. 9 b) when moving from the larger particles to nanosized ones. The value of this blue shift is near 830 cm^{-1} and may correspond to the increase of the Fe_2O_3 band gap due to the size quantization effect.[36] This phenomenon is likely the case for the ferric clusters consisting the zeolite taking into account the size of these particles which is in the range of 2-3 nm for microbeads and can be visualized by TEM analyses (Fig. 9 b), but less than 1 nm for nanobeads and invisible by TEM (Fig. 2 a).

The acidity of Fe-silicalite materials was investigated by means of temperature programmed desorption (TPD) of NH_3. The TPD spectra of ammonia for zeolite bodies built of Fe-silicalite nanobeads are conformed and exhibit both *l*- and *h*-peaks at about 450 and 620 K, respectively (Fig.10). The high temperature peak is related to the ammonia desorption from strong Brønsted and Lewis sites, which are usually of catalytic importance.[37]

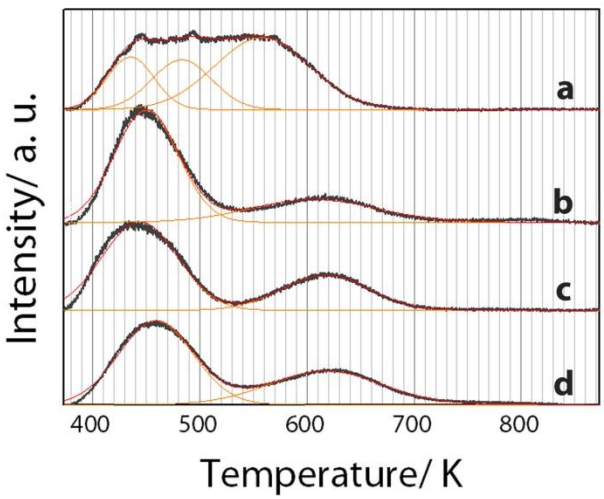

Fig. 10. Ammonia TPD profile of Fe-silicalite microbeads (a) and zeolite materials with spongy (b), random (c) and close (d) packing of nanobeads.

The overlapping peaks were deconvoluted into Gauss functions (Fig. 10) and the absolute number of strong acid sites was quantified by integrating the area of the peak at about 620 K (Table 1). Among the nanozeolite materials the most narrow and intense *h*-peak is observed for randomly packed nanobeads, indicating the most distinct distribution of strong acid sites. For close packed nanobeads, the presence of clearly defined shoulder in the 700-800 K temperature region is observed indicating the presence of some number of very strong Lewis sites on the sample.

The TPD spectrum of NH_3 for Fe-silicalite microbeads differ from other spectra, acid sites of medium strength can be noticed in the TPD profile, there is an additional peak at lower temperature with comparison to nanocrystalline materials. This additional peak at 490 K may be ascribed to ammonia desorption from Lewis acid sites on Fe_2O_3[38,39] presenting as 2-3 nm ferric clusters consisting the microbeads. Both *l*- and *h*-peaks shift to the lower desorption temperatures 430 and 560 K, respectively, indicating a weakening of acid sites related to the zeolite surface as compared with nanocrystalline samples. The total NH_3 adsorption capacity of zeolite microbeads is nearly the same as that of nanozeolite bodies based on the amount of iron (see Table 1).

Hierarchically porous materials built of Fe-silicalite nanobeads and reference sample of Fe-silicalite microbeads were tested in catalytic oxidation of macrolide antibiotic – clarithromycin lactobionate. Macrolide antibiotics have been emerged in aquatic environment worldwide[11,40] because of high excretion rates of unchanged antibiotics molecules (>60%)[41] and low elimination of these drugs in sewage treatment plants.[42]

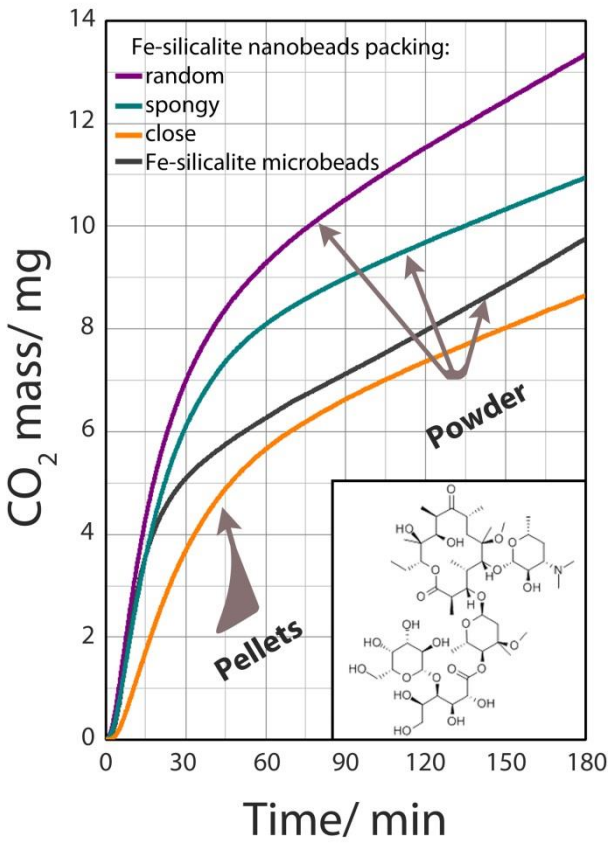

Fig. 11. Kinetic curves of CO_2 emission during CL total oxidation by H_2O_2 at 323 K, $[H_2O_2]_0$ = 1 M, $[CL]_0$ = 300 mg/L, $[catalyst]_0$ = 20 g/L, $V_{liquid\ phase}$ = 50 ml, $d_{pellets}$ = 1.25-2 mm. The inset shows chemical formula of the antibiotic – clarithromycin lactobionate.

Table 2. Catalytic properties of Fe-silicalite materials at 323 K, $[H_2O_2]_0$ = 1 M, $[catalyst]_0$ = 20 g/L, $V_{liquid\ phase}$ = 50 ml.

Fe-silicalite sample	pH	Initial H_2O_2 decomposition rate (W_0), mg_{O_2}/min $[CL]_0 = 0$	Initial H_2O_2 decomposition rate (W_{CL}), mg_{O_2}/min $[CL]_0$ = 300 mg/L	The contribution of CL oxidation process $(W_0-W_{CL})/W_0$, %	Initial CO_2 emission rate, mg_{CO_2}/min	CL conversion in 3 h, %
Microbeads	4.5	46	41	11	0.33	32
Nanobeads random packing	3.0	63	47	25	0.36	44
Nanobeads close packing	3.0	33	24	27	0.13	28
Nanobeads spongy packing	3.0	58	49	16	0.30	36

Typical kinetic curves of CO_2 emission during the total oxidation of high molecular weight CL (M_w = 1088 g/mol) in heterogeneous Fenton systems Fe-silicalite/H_2O_2 at 323 K are represented in Fig. 11. Kinetic curves for powder catalysts observed to have different shapes for nanobeads and microbeads, lower CL conversion was achieved for Fe-silicalite microbeads vs nanozeolite catalysts at relatively high initial CO_2 emission rate (Table 2). To explain this phenomenon, initial hydrogen peroxide decomposition rates in the presence and absence of CL were measured barometrically (Table 2). The relative difference between the rates shows the contribution of targeting reaction between CL and ȮH-radicals. The contribution of CL oxidation reaction is higher for nanozeolite catalysts vs Fe-silicalite microbeads (Table 2), demonstrating the positive effect of high surface accessibility. Decreasing Fe-silicalite crystal size promotes the enhanced interaction between adsorbed substrate and ȮH-radicals generated on Fe-containing catalytic sites and reduces contribution of non-targeting ȮH radicals consumption by H_2O_2 with O_2 emission inside micropores.

Pellets built of closely packed Fe-silicalite nanobeads seemed to be mechanically stable during CL oxidation reaction despite of intensive O_2 bubbles flow escaping through catalyst pores. Both rates of O_2 and CO_2 emission and CL conversion is lower for nanozeolite pellets vs other catalysts (Figure 12, Table 2). This fact can be explained by particular experiments when the reaction rates are measured by the gas emission. Slower formation of gaseous bubbles inside the pellets compared with powder catalysts may result in slower gas emission. However a possible role of mesopores with the size >40 nm for catalytic oxidation of high molecular weight substrate by hydrogen peroxide, as well as differences in iron catalytic centers cannot be denied. More systematic catalytic experiments for all systems described here with detailed discussion of the reaction mechanisms will be presented in the next publication.

Conclusions

Hierarchically porous Fe-silicalite materials with desired texture were synthesized by two approaches: patterning the initial building nanozeolite blocks and embedding additional macropores using supramolecular template during zeolite crystallization. Fe-silicalite materials built of close and random packed uniform nanozeolites were formed by the centrifugation and sedimentation of nanozeolite suspension, respectively, followed by drying and calcination. Micro/meso/macroporous Fe-silicalite material with spongy texture with walls built of closely packed nanocrystals was designed using polystyrene latex as supramolecular template. All hierarchical zeolites exhibit good XRD crystallinity and high BET surface area (369-550 m^2/g) and high specific pore volume (0.63-0.75 cm^3/g). Fe-silicalite pellets built of closely packed nanocrystals have narrow mesopore size distribution with a sharp maximum at 25 nm. Fe-silicalite material built of randomly packed nanozeolites has bimodal mesoporosity with maximums at 30 and 45 nm, while Fe-silicalite material with spongy packing of nanobeads form monomodal mesoporosity with a maximum at 30 nm. Calcined Fe-silicalite materials built of nanobeads contain uniformly distributed ferric clusters no more than 1 nm in size, while for Fe-silicalite microbeads clusters size is 2-3 nm. Nanozeolite materials have weak and strong Brønsted and Lewis sites with total concentration of 0.12-0.16 mmol/g. The 3 nm-ferric clusters in zeolitic microbeads resulted in the appearance of Lewis acid sites with medium strength, which are absent in nanobeads, and a weakening of the zeolite acidity compared with nanobeads. Fe-silicalite pellets built of closely packed nanobeads show a good mechanical stability in benzene and water. Catalytic performance of hierarchical Fe-silicalites in total oxidation of high MW antibiotic – clarithromycin lactobionate by hydrogen peroxide was enhanced vs Fe-silicalite microbeads due to increasing catalytic sites accessibility. Pellets built of closely packed Fe-silicalite nanobeads were mechanically stable during CL oxidation reaction. New nanocrystalline Fe-silicalites are promising catalysts for total and partial oxidation of high MW molecules.

Acknowledgements

The work was performed in the framework of Skolkovo Foundation (Grant Agreement for Russian educational organization №1 on 28.11.2013). The synthetic and analytic experiments were financed by RSFC grant 14-13-01155 and RFBR grant 12-03-93116_a, respectively.

Notes and references

[a] *Boreskov Institute of Catalysis SB RAS, 5 Lavrentieva st., Novosibirsk 630090, Russia*

[b] *Novosibirsk State University, 2 Pirogova st., Novosibirsk 630090, Russia*

[c] *Research and Education Centre, NSU, 2 Pirogova st., Novosibirsk 630090, Russia*

† Electronic Supplementary Information (ESI) available: video "Pellets in benzene" show diffusion of benzene from the edge to the centre of the Fe-silicalite pellets built of closely packed nanobeads. The pellets retain their sharp becoming transparent, sometimes pellets crack due to the large pressure drops. This material is available free of charge via the Internet at http://www.rsc.org/

1 A. Corma, *Journal of Catalysis*, 2003, **216**, 298.
2 I. W. C. E. Arends, R. A. Sheldon, *Applied Catalysis A: General*, 2001, **212**, 175.
3 K. Moiler, D. C. Koningsberger, T. Bein, *J. Phys. Chem.*, 1989, **93**, 6116.
4 C. Hammond, M. M. Forde, M. H. Ab Rahim, A. Thetford, Q. He, R. L. Jenkins, N. Dimitratos, J. A. Lopez-Sanchez, N. F. Dummer, D. M. Murphy, A. F. Carley, S. H. Taylor, D. J. Willock, E. E. Stangland, J. Kang, H. Hagen, C. J. Kiely, G. J. Hutchings, *Angew. Chem. Int. Ed.*, 2012, **51**, 5129.
5 M. M. Forde, R. D. Armstrong, C. Hammond, Q. He, R. L. Jenkins, S. A. Kondrat, N. Dimitratos, J. A. Lopez-Sanchez, S. H. Taylor, D. Willock, C. J. Kiely, G. J. Hutchings, *J. Am. Chem. Soc.*, 2013, **135**, 11087.
6 S. Navalon, M. Alvaro, H. Garcia, *Applied Catalysis B: Environmental*, 2010, **99**, 1.
7 G. Centi, S. Perathoner, T. Torre, M. G. Verduna, *Catalysis Today*, 2000, **55**, 1‑2, 61.
8 S. Bayen, H. Zhang, M. M. Desai, S. K. Ooi, B. C. Kelly, *Environmental Pollution*, 2013, **182**, 1.
9 C. Fernández, M. González-Doncel, J. Pro, G. Carbonell, J.V. Tarazona, *Science of the Total Environment*, 2010, **408**, 543.
10 Y. Valcárcel, S. González Alonso, J. L. Rodríguez-Gil, A. Castaño, J. C. Montero, J. J. Criado-Alvarez, I. J. Mirón, M. Catalá, *Environ Sci Pollut Res*, 2013, **20**, 1396.
11 D. Bendz, N. A. Paxéus, T. R. Ginn, F. J. Loge, *Journal of Hazardous Materials*, 2005, **122**, 195.
12 Q. Yan, X. Gaoa, Y.-P. Chen, X.-Y. Peng, Y.-X. Zhang, X.-M. Gan, C.-F. Zi, J.-S. Guo, *Science of the Total Environment*, 2014, **470–471**, 618.
13 K. A. Sashkina, V. S. Labko, N. A. Rudina, V. N. Parmon, E. V. Parkhomchuk, *Journal of Catalysis*, 2013, **299**, 44.
14 J. Pérez-Ramírez, C. H. Christensen, K. Egeblad, C. H. Christensen, J. C. Groen, *Chem. Soc. Rev.*, 2008, **37**, 2530.
15 V.Valtchev, L.Tosheva, *Chem. Rev.*, 2013, **113**, 6734.
16 K. Möller, T. Bein, *Chem. Soc. Rev.*, 2013, **42**, 3689.
17. D. P. Serrano, J. M. Escola, P. Pizarro, *Chem. Soc. Rev.*, 2013, **42**, 4004.
18. M. E. Davis, *Nature*, 2002, **417**, 813.
19. S. Cai, D. Zhang, L. Shi, J. Xu, L. Zhang, L. Huang, H. Li, J. Zhang, *Nanoscale*, 2014, **6**, 7346.
20 K. H. Rhodes, S. A Davis, F. Caruso, B. Zhang, S. Mann, *Chem. Mater.*, 2000, **12**, 2832.
21 V. Valtchev, *Chem. Mater.*, 2002, **14**, 956.
22 Y. Shi, X. Li, J. Hu, J. Lu, Y. Ma, Y. Zhang, Y. Tang, *J. Mater. Chem.*, 2011, **21**, 16223.
23 S. Mintova, M. Hölzl, V. Valtchev, B. Mihailova, Y. Bouizi, T. Bein, *Chem. Mater.*, 2004, **16**, 5452.
24 D. Zou, L. Sun, J. J. Aklonis, R. Salovey, *Journal of Polymer Science: Part A; Polymer Chemistry*, 1992, **30**, 1463.
25 S. J. Gregg, K. S. W. Sing, Adsorption, surface area, and porosity. Academic Press. 1982.
26 E. P. Barrett, L. G. Joyner, P. P. Halenda, *J. Amer. Chem. Soc.*, 1951, **73**, 373.
27 J. Landers, G. Yu. Gor, A. V. Neimark, *Colloids and Surfaces A: Physicochemical and Engineering Aspects*, 2013, **437**, 3.
28 M. Jaroniec, M. Kruk, J. P. Olivier, *Langmuir*, 1999, **15**, 5410.
29 M. Kruk, M. Jaroniec, *Chemistry of Materials*, 2000, **12**, 222.
30 A. Saito, H. C. Foley, *Microporous Mater.*, 1995, **3**, 543.
31 P. L. Llewellyn, J. P. Coulomb, Y. Grillet, J. Patarin, H. Lauter, H. Reichert, J. Rouquerol, *Langmuir*. 1993, **9**, 1846.
32 S. Bordiga, R. Buzzoni, F. Geobaldo, C. Lamberti, E. Giamello, A. Zecchina, G. Leofanti, G. Petrini, G. Tozzola, G. Vlaic, *Journal of catalysis*, 1996, **158**, 486.
33 J. Pérez-Ramírez, J. C. Groen, A. Brückner, M. S. Kumar, U. Bentrup, M. N. Debbagh, L. A. Villaescusa, *Journal of Catalysis*, 2005, **232**, 318.
34 P. Ratnasami, R. Kumar, *Catalysis Today*, 1991, **9**, 4, 357.
35 K. A Sashkina, E. V Parkhomchuk, N. A. Rudina, V. N. Parmon, *Microporous and Mesoporous Materials*, 2014, **189**, 181.
36 L. J. Brus, Chem. Phys., 1984, 80, 4403.
37 N. Katada, T. Miyamoto, H. A. Begum, N. Naito, M. Niwa, A. Matsumoto, K. Tsutsumi, *J. Phys. Chem. B*, 2000, **104**, 5511.
38 S. Wagloehnera, J. N. Baerb, S. Kureti, *Applied Catalysis B: Environmental*, 2014, **147**, 1000.
39 C. Wang, S. Yang, H. Chang, Y. Peng, J. Li, *Journal of Molecular Catalysis A: Chemical*, 2013, **376**, 13.
40 Y. Valcárcel, S. González Alonso, J. L. Rodríguez-Gil, A. Gil, M. Catalá, Chemosphere, 2011, 84, 1336–1348.
41 R. Hirsch, , T.A.Ternes, , K. Haberer, A.Mehlich, , F. Ballwanz, , K.-L.Kratz, J. Chromatogr. A, 1998, 815, 213–223.
42 Q. Yan, X. Gao, L. Huang, X.-M. Gan, Y.-X. Zhang, Y.-P. Chen, X.-Y. Peng, J.-S. Guo, Chemosphere, 2014, 99, 160.